ELSEVIER

Journal of Alloys and Compounds 279 (1998) 171–178

Journal of ALLOYS AND COMPOUNDS

Molecular dynamics simulations of the self-diffusion phenomena in Ni_2Y intermetallic phase

Kan Hachiya*, Yasuhiko Ito

Department of Fundamental Energy Science, Kyoto University, Kyoto 606-8501, Japan

Received 11 December 1997; received in revised form 27 April 1998

Abstract

We present a molecular dynamics study of the diffusion phenomena in Ni_2Y, transition-metal intermetallic phase via nearly-free-electron–tight-binding-bond interatomic interaction model. Interpretations of the dynamic structures from the calculations of the mean square displacements and spectral densities of velocity show that the rapid growth of this intermetallic phase found in the experimental study is mainly due to the high-rate self-diffusion in and near the grain-boundaries and independent of the vacancy. Therefore, the standard vacancy-based diffusion process is found to be not essential in this phase.

Keywords: Molecular dynamics; Diffusion; Intermetallic compound; Laves phase

1. Introduction

The acceleration of the atomic transport in the solid state materials is often one of the central problems in energy conversion processes. Diffusion, very often, determines the speed of the atomic transport, and therefore determines the efficiency.

Ni_2Y is the transition-metal intermetallic compound with cubic Laves phase structure and its anomalously high growth rate in electrolysis was found by one of the present authors by electrochemical experiments [1]. The Ni–Y intermetallic compound is formed by electrodeposition of Y at the Ni electrode in the molten LiCl–KCl–NaCl–YCl_3, and the Ni_2Y phase selectively grows among competing phases with the growth rate of 10 $\mu m\, h^{-1}$ at 773 K, which is 600 K below the melting point.

This high growth rate means that the speed of the atomic transport for the atomic species in this intermetallic phase is of the order of 10^{-12} $m^2\, s^{-1}$ as the diffusion coefficient [1]. This is comparable to, or only few orders smaller than those in the standard liquid phase, which are approximately 10^{-9} $m^2\, s^{-1}$ as the diffusion coefficient, or in the common solid phase near melting point, which is 10^{-11} $m^2\, s^{-1}$ [2].

How can such anomalously rapid growth of the intermetallic phase take place? There are several models to describe the atomic diffusion in standard solids; diffusion process via vacancy, dislocation, grain boundary, and so on [3]. To which model is the diffusion process in this phase ascribed?

We studied the microscopic dynamic structure of Ni_2Y phase through atomistic simulation, a molecular dynamics simulation, in the investigation of the high growth rate of this intermetallic phase.

Concerning the molecular dynamics technique, a semi-empirical method for the interatomic potential calculation has recently been developed [4] and a wide range of materials has come into applicability of the atomistic simulation. Chemical bondings in transition-metal alloy compounds is well-described within the NFE–TBB (nearly-free-electron–tight-binding-bond) framework [5] and its TBB part can be calculated by the semi-empirical method exact enough to express the many-atom character of interactions in transition-metal intermetallic compounds and computationally fast enough to be used in the intensive molecular dynamics run.

In the present article, the calculation of pair potential with the application of the NFE–TBB many-atom interaction model is demonstrated and then used for the calculation of the many-body forces in molecular dynamics calculation.

The computational methods used are outlined in Section 2. The results of the applications to the self-diffusive motion in vacancy, grain-boundary structures for Ni_2Y are

*Corresponding author.

0925-8388/98/$ – see front matter
PII: S0925-8388(98)00647-1

shown in Section 3. We present our conclusions in Section 4.

Throughout this article, we use atomic units, and energies are given in rydberg where not indicated.

2. Computational method

2.1. Interatomic potential

For the interatomic potential for Ni_2Y, we use the NFE–TBB expression developed by Hausleitner and Hafner [5]. In their approach, the total energy is given as the sum of a volume energy and the sum of the following interatomic potential;

$$\Phi_{\mathrm{tot}} = \Phi_{\mathrm{sp}} + \Phi_{\mathrm{d,rep}} + \Phi_{\mathrm{d,bond}}. \quad (1)$$

The potential energy is divided into free-electron-like interaction, pairwise repulsive interaction and many-atom attractive bond energy.

We adopt the following NFE interaction formulation by Pettifor and Ward [6] as the first term in Eq. (1);

$$\Phi_{\mathrm{sp},ij} = \frac{2N_{\mathrm{s},i}N_{\mathrm{s},j}}{r_{ij}} \sum_{n=1}^{3} A_n \cos(k_n r + \alpha_n) \exp(\kappa_n r_{ij}). \quad (2)$$

$N_{\mathrm{s},i}$ is the number of sp-valence electrons for the i atom. Calculated parameters for the perfect Ni_2Y crystal are compiled in Table 1. As in Ref. [6], Ashcroft empty core pseudopotential [7] is used to calculate these parameters. The parameters in Table 1 are calculated from the empty core radius, $r_c = 0.652$ Å (Ni–Ni), 0.834 Å (Ni–Y) and 0.881 Å (Y–Y). These values are chosen such that the position of the first potential minima fit the crystallographic interatomic spacings, respectively.

The remaining two terms in Eq. (1) are described within the tight-binding theory [8].

Repulsive interaction is known to be proportional to r^{-10}, the square of hopping integral, but in this study, r^{-8} form is used as in Ref. [9]. The following is the repulsive interaction used;

$$\Phi_{\mathrm{rep},ij} = \frac{\sqrt{N_{\mathrm{d},i}N_{\mathrm{d},j}}}{7} \frac{h_{ij}^2 d_{ij}^{10}}{r_{ij}^8}. \quad (3)$$

h_{ij} is the bond integral and it is calculated in the same way as in Ref. [10]. d_{ij} is the interatomic spacings. The calculated h_{ij} values for the Ni_2Y are as follows; $h_{\mathrm{NiNi}} = 0.01964$ Ry, $h_{\mathrm{NiY}} = 0.02938$ Ry, $h_{\mathrm{YY}} = 0.07843$ Ry.

Table 2
Bond order for covalent d–d interactions in the Ni_2Y phase within the angular dependent second moment approximation

	σ	π	δ
Θ_{NiNi}	0.4612	0.2906	0.0672
Θ_{NiY}	0.3131	0.1908	0.0488
Θ_{YY}	0.4901	0.4074	0.1434

Bond energy expression is;

$$\Phi_{\mathrm{bond},ij} = 2 \sum_{\alpha\beta} H_{j\beta,i\alpha} \Theta_{i\alpha,j\beta}. \quad (4)$$

$H_{j\beta,i\alpha}$ is the tight-binding Hamiltonian and $\Theta_{i\alpha,j\beta}$ is the bond order. Bond order is calculated from the following simplified expression derived by Pettifor and Aoki [11];

$$\Theta_{i\alpha,j\beta} = 2 \sum_{n=2}^{\infty} \hat{\chi}_n(N_{\mathrm{d}}) \zeta_n^r / b^{n-1}. \quad (5)$$

$\hat{\chi}_n$ (N_{d}) is the reduced susceptibility, ζ_n^r is the interference term in the ring approximation and b is the square root of the second moment μ_2, calculated from the tight-binding Hamiltonian [12]. The calculated bond order for each bonding in the perfect Ni_2Y crystal with Eq. (5) within the second moment approximation is compiled in Table 2, and up to the sixth moment approximation results are presented in Fig. 1.

The major points that are different from the original NFE–TBB model by Hausleitner and Hafner [5] are as follows:

- Analytical expression by Pettifor and Ward [6] is chosen for the NFE term for the faster computations;
- Bond order is calculated by the model by Pettifor and Aoki [11] and each σ, π and δ orbital is treated separately;
- Bond order is calculated not only with the crystallographic configuration but with the configuration at every molecular-dynamics time step where indicated. If the bond order is calculated at every step, the tight-binding attractive force has a many-body character while it is pairwise at last for the fixed bond order.

Table 1
NFE potential parameters for the Ni_2Y perfect crystal. The values are indicated in a.u.

n	Ni–Ni			Ni–Y			Y–Y		
	1	2	3	1	2	3	1	2	3
k_n	0.303	1.144	1.695	0.320	0.901	1.285	0.291	0.731	0.995
κ_n	1.415	1.227	0.494	1.134	0.897	0.371	0.919	0.671	0.283
A_n	8.586	1.533	0.039	5.818	1.566	0.045	2.567	0.948	0.026
α_n	−1.407	−3.785	1.154	−1.297	−3.470	1.346	−1.022	−2.651	2.543

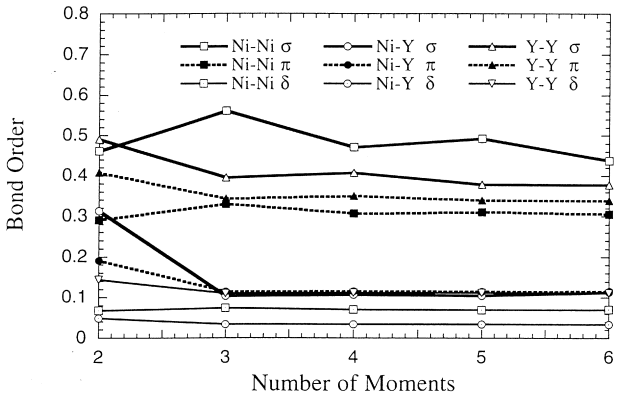

Fig. 1. Dependence of the bond order for the bondings in the bulk structure to the number of moments.

N_d in the above expressions is derived using the rectangular band model for d bands [13] and N_s is derived regarding the rest of the valence electrons as sp valence electrons. Local charge neutrality is imposed upon each Ni and Y atoms and the site-diagonal energy shift is calculated within the tight-binding-Hartree–Fock approximation following Ref. [5];

$$\Delta N_{s,\alpha} + \Delta N_{d,\alpha} = 0, \quad (\alpha = \mathrm{Ni, Y}) \tag{6}$$

$$x_{\mathrm{Ni}} \Delta N_{d,\mathrm{Ni}} + x_Y \Delta N_{d,\mathrm{Y}} = 0 \tag{7}$$

$$\Delta E_\alpha = u_{dd} \Delta N_{d\alpha} + u_{sd} \Delta N_{s,\alpha} + V\sigma Z(\Delta N_{d,\alpha} + \Delta N_{s,\alpha}). \tag{8}$$

ΔN_s and ΔN_d are the shift of the number of s and d valence electrons from arbitrary initial values. In this calculation, $N_{s,\mathrm{Ni}} = 1.40$, $N_{d,\mathrm{Ni}} = 8.60$, $N_{s,\mathrm{Y}} = 1.31$ and $N_{d,\mathrm{Y}} = 1.69$ for pure Ni and Y [5] are used as initial values, and the standard values from the literature [14] are used for the parameters in Eq. (8) as in Ref. [5]. x_α is the concentration of α atom. ΔN_s and ΔN_d are determined such that Eqs. (6)–(8) are self-consistent. The final values for Ni and Y in Ni_2Y phase are as follows; $N_{s,\mathrm{Ni}} = 1.65$, $N_{d,\mathrm{Ni}} = 8.35$, $N_{s,\mathrm{Y}} = 0.81$ and $N_{d,\mathrm{Y}} = 2.19$.

For the calculations for Ni–Y interaction, $\sqrt{N_{\mathrm{Ni}} N_{\mathrm{Y}}}$ is used instead of N_α where needed.

The only adjustable parameter is r_c for Eq. (2). As mentioned below, this is adjusted to reproduce interatomic spacings. So far, as we know, no experimental values are available for the cohesive energy or for the vacancy formation energies. So, we have not checked the validity of this model other than the fitted interatomic spacings.

In Fig. 2 the total NFE–TBB effective interatomic potentials given by Eq. (1) at a reference crystallographic crystal structure (C15) are shown.

2.2. Molecular dynamics calculation

We used the constant temperature Nosé–Hoover equations of motion for the present molecular dynamics calculations [15,16];

$$m_i \dot{\boldsymbol{v}}_i = \boldsymbol{F}_i - \zeta m_i \boldsymbol{v}_i \tag{9}$$

$$\dot{\zeta} = 2(K - K_0)/Q, \tag{10}$$

where K is the kinetic energy of the system and K_0 is the kinetic energy corresponding to the desired temperature. The temperature is set to 773 K throughout the present study.

The molecular dynamics simulations for the present study have the following initial conditions:

- Perfect crystal;
- Crystal structure with vacancy;
- Crystal structure with grain-boundary.

Details of each condition is presented in the corresponding subsection in the Section 3.

For all conditions, Q is set to 1.000×10^9 a.u. except for the grain-boundary conditions, $Q = 1.189 \times 10^5$ a.u. Determined Q is such that the fluctuations of the total kinetic and potential energy are small, so as not to violate the crystal structure by a sudden jump of the temperature of the simulated system. The adopted values are much larger

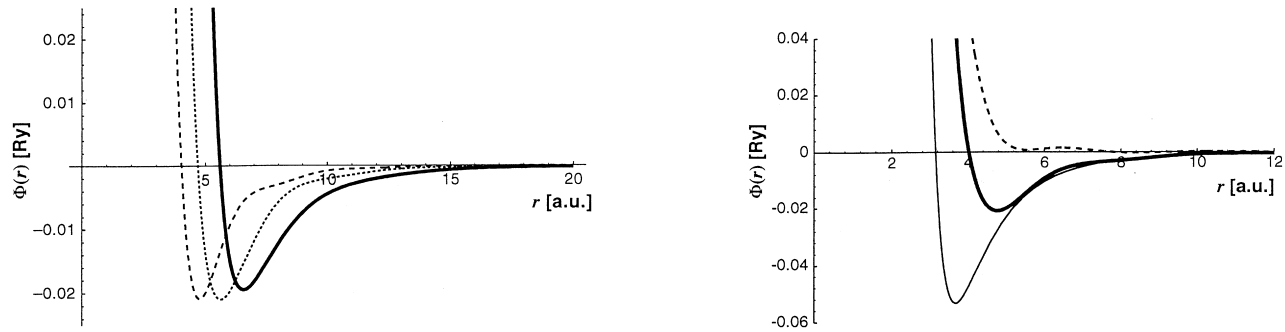

Fig. 2. Effective interatomic potential for Ni–Ni, Ni–Y and Y–Y interactions (left). The dashed line is for the Ni–Ni interaction, the dotted line is for the Ni–Y interaction and the solid line is for the Y–Y interaction. The interatomic potential for sp (Eq. (2)) and d (Eqs. (3) and (4)) interactions for Ni–Ni (right). The dashed line is for the sp interaction, the thin solid line is for the d interaction and the bold solid line is for the total interaction.

than those characterized by Holian et al. [17]. Therefore, for conditions other than the grain-boundary condition, the systems are weakly-coupled, although for the grain-boundary condition, the simulated system is coupled to the thermostat with the response time corresponding to the Einstein frequency.

For the calculation of the self-diffusion coefficient, the Einstein relation for the diffusion coefficient [18] is used;

$$D = \lim_{t\to\infty} \langle |\boldsymbol{r}(t) - \boldsymbol{r}(0)| \rangle / 6t. \tag{11}$$

Self-diffusion coefficients are evaluated from mean square displacement plots against time.

The autocorrelation function and the spectral density of velocity $\boldsymbol{v}(t)$ are [18];

$$C(t) = \langle \boldsymbol{v}(t) \cdot \boldsymbol{v}(0) \rangle \tag{12}$$

$$I(\omega) = 2 \int_0^\infty C(t) \cos\omega t \, \mathrm{d}t. \tag{13}$$

3. Results and discussions

3.1. Perfect crystal calculation

For the initial configuration, $3\times3\times3$ crystallographic unit cells, i.e. 432 Ni atoms and 216 Y atoms are set in the simulation supercell. Bond order is calculated applying Eq. (5) to the initial reference crystallographic structure. The many-body attractive force is then replaced by the sum of the pairwise attractive force. Equations of motion are integrated numerically with leap-frog method [19], over 10 000 steps after 5000 equilibration steps with $\Delta t = 1.0\times10^{-15}$ s and the force calculation is cut off at 7.181 Å, which is the same as the lattice constant for Ni_2Y.

In Fig. 3 the radial distribution function for Ni–Ni at 773 K is shown. Sharp peaks show that the perfect crystal structure for Ni_2Y is well reproduced by molecular dynamics. No diffusive motion is observed and very small numbers of vibrational modes are visible. The frequencies of the modes clearly visible are almost the same for both Ni and Y, as in Figs. 4 and 5.

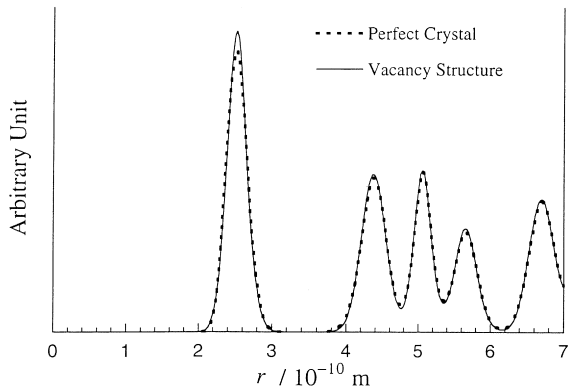

Fig. 3. Radial distribution functions for Ni–Ni at 773 K. The dashed line shows the distribution in the perfect crystal and the solid line shows the distribution in the Ni vacancy structure.

3.2. Vacancy structure calculation

We adopt the structures the same as presented in Section 3.1 with one Ni vacancy and two Ni vacancies formed in the unit cell at the centre as the two initial configurations for vacancy structure simulations. The two vacancies are separated from each other for more than a third-nearest-neighbour distance not to form another vacancy. The numerical conditions are the same as in Section 3.1 for both, except the number of steps, which is 18 000 for the two-vacancies structure.

The choice of Ni vacancy is due to the results of the estimation of the vacancy formation energy which show that the formation energy for the Ni vacancy is 0.23 Ry, which is half as small as that for the Y vacancy, 0.45 Ry [20]. These values roughly correspond to the concentration of vacancies around 10^{-20}. In the first place, this means that the vacancies are hard to form in this phase.

The radial distribution function for the Ni–Ni pair at 773 K for the one-vacancy condition is shown in Fig. 3. Compared with the perfect crystal structure, there are almost no differences observed in all of the Ni–Ni, Ni–Y and Y–Y distribution curves. The reference crystallographic Ni_2Y structure is also well reproduced in the vacancy structure simulation. Mean square displacements are given in Fig. 4 for the one-vacancy condition and no diffusive motion is observed within 10 000 times steps. This is also the case for the two-vacancies condition within 18 000 time steps. Spectral density curves are given in Figs. 5 and 6. Both the one-vacancy and the two-vacancies structures have a similar sharp peaks structure but the frequency of the main peaks are shifted from that of the perfect crystal in the two-vacancies condition. Again, no

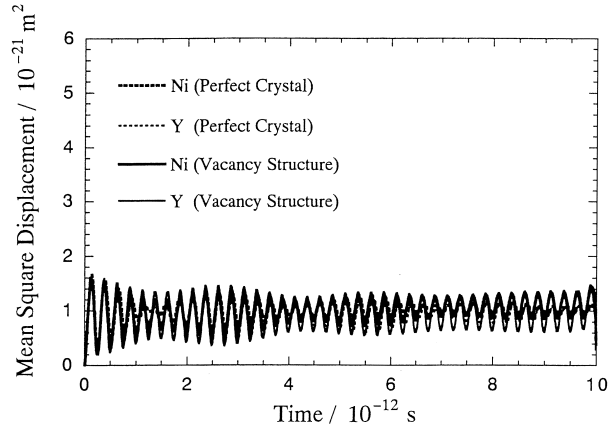

Fig. 4. Mean square displacements (MSD) at 773 K. The dashed line shows the MSD in a perfect crystal and the solid line shows the MSD in a Ni vacancy structure. The bold lines represent Ni and the thin lines represent Y.

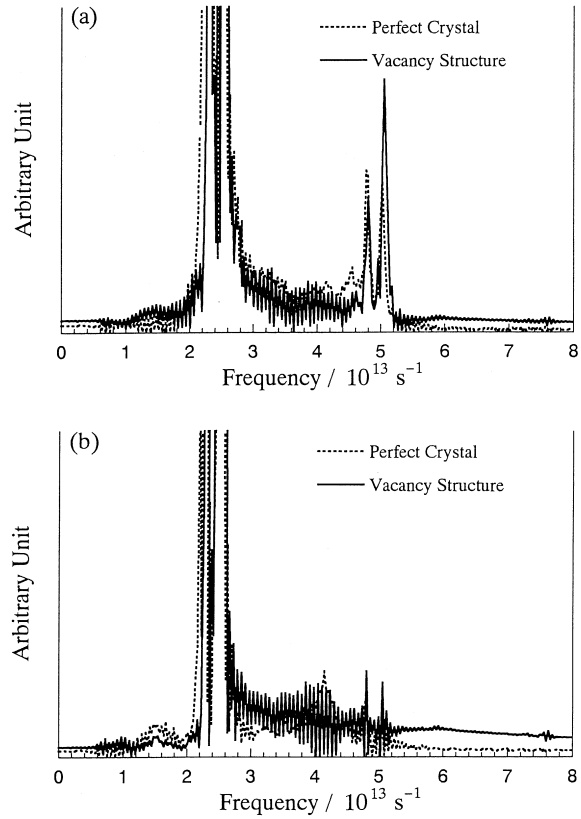

Fig. 5. Spectral densities of velocity for Ni (a) and Y (b) at 773 K. The dashed line is for a perfect crystal and the solid line is for a Ni vacancy structure.

diffusive mode is observed for both one-vacancy and two-vacancy conditions.

The direct many-body attractive force calculation in Eq. (5) is also performed for the one Ni vacancy initial condition over 7000 time steps. The conditions for this simulation are the same as in the pairwise force calculation. No diffusive motions are observed again, both in the mean square displacements and in the spectral densities.

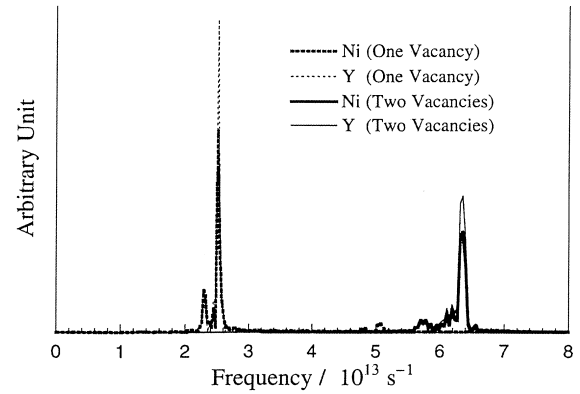

Fig. 6. Spectral densities of velocity for Ni and Y at 773 K. The dashed line is for a one-vacancy structure shown in Fig. 5 and the solid line is for a two-vacancies structure. The bold lines represent Ni and the thin lines represent Y.

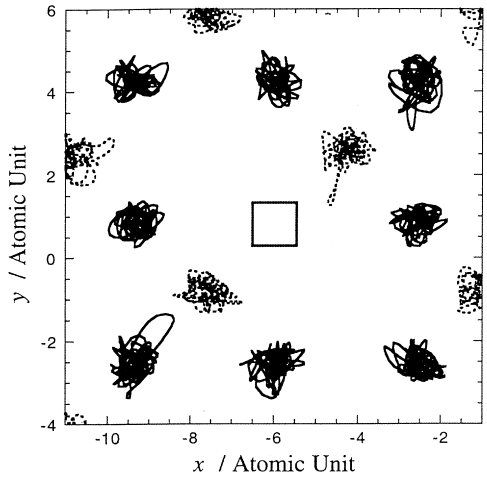

Fig. 7. Examples of the atomic motions near the Ni vacancy projected onto a two dimensional plane. The solid lines show Ni trajectories and the dashed lines show Y trajectories. The open square represents a Ni vacancy.

An example of the atomic motions near the Ni vacancy are shown in Fig. 7. Both Ni and Y atoms fluctuate around their initial atomic position and no jump motion is observed. Initial regular atomic arrangements are conserved even for the atoms neighbouring the vacancy.

3.3. Grain-boundary structure calculation

In order to take the effect of the grain-boundary into account, a symmetric tilt boundary model containing 1080 (720 Ni and 360 Y) atoms with $\theta = 0.3218$ rad is used for the initial configuration. The choice of this particular initial condition is only due to the demand from the simulation supercell and we do not know any experimental grain-boundary structures to compare with this model. For initial coordinates, atoms are arranged as shown in Fig. 8. The cell contains 432 (288 Ni and 144 Y) fixed atoms.

The computational conditions for this calculation are different in order to achieve faster computation per atom. This is because more atoms are set in the simulation unit cell and the many-atom attractive force calculation is used for anisotropic and inhomogeneous atomic arrangements. The equations of motions are integrated with the Størmer algorithm [21] over 10 000 time steps after 5000 equilibration steps with $\Delta t = 1.0 \times 10^{-15}$ s. The force cut off lengths are set to 5.027 Å for Ni–Ni, 5.821 Å for Ni–Y and 6.350 Å for Y–Y (9.500, 11.00 and 12.00 in a.u., respectively). To determine these cut off lengths, we have confirmed the correspondence of the radial distribution function and the mean square displacements plot versus time between those calculated using these cut off lengths and those calculated using cut off lengths for other conditions (7.181 Å) by preliminary 2000 steps calculation. The estimated error in the calculation of the diffusion coefficients, which arises from the choice of these shorter cut off lengths, is 1%.

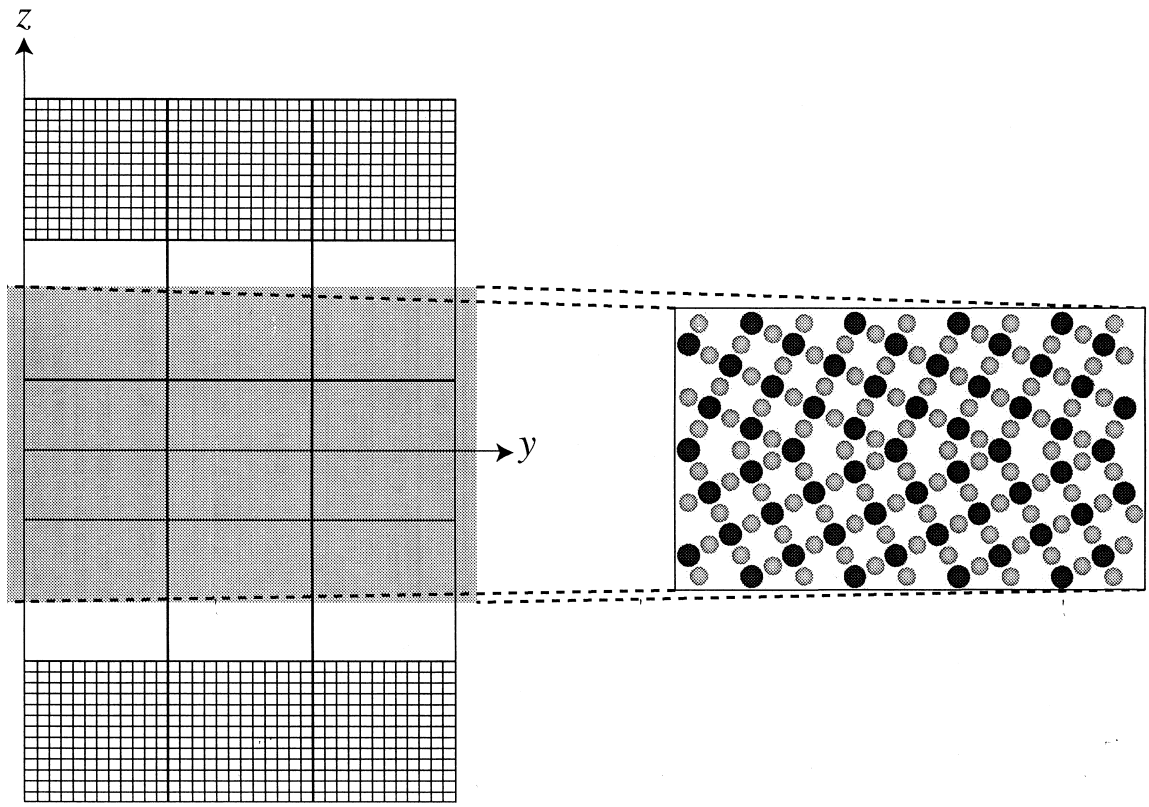

Fig. 8. The model for molecular dynamics simulation for a grain-boundary structure in the Ni_2Y phase. The schematic of the computational cell and the projected atomic arrangements. The periodic boundary conditions are posed on all borders except on the z borders. The squares, in grids, correspond to the unit cell. Meshed regions correspond to the unit cells containing fixed atoms.

That is, the same diffusive motions, that we describe as follows, are also observed in the 2000 steps calculation with the cut off lengths of other conditions, and the results obtained with the possible longer time steps calculation are also expected to be the same, as follows.

The data analysis in this condition is done using 100 sample coordinates out of 10 000 time steps coordinates chosen at every 100th steps. In Fig. 9 the horizontal and vertical mean square displacements in the following definitions of the corresponding diffusion coefficients are shown;

$$D_{x^2+y^2} = \lim_{t\to\infty} \langle |x(t) - x(0)|^2 + |y(t) - y(0)|^2 \rangle / 4t \qquad (14)$$

$$D_{z^2} = \lim_{t\to\infty} |z(t) - z(0)|^2 / 2t \qquad (15)$$

$D_{x^2+y^2}$, which characterizes the diffusivity of the horizontal motion in the plane parallel to the grain-boundary, is the self-diffusion coefficient calculated from the horizontal mean square displacement and D_{z^2}, which characterizes the diffusivity of the vertical motion to the grain-boundary plane, is the self-diffusion coefficient calculated from the vertical mean square displacement, for the grain-boundary is $z=0$. Both horizontal and vertical mean square displacements increase monotonously with time and therefore the diffusive motion can be clearly observed and we can calculate $D_{x^2+y^2}$ and D_{z^2} with these curves by the least-square fitting to the linear functions. The calculated self-diffusion coefficients are $D_{x^2+y^2} = 6.695\times10^{-11}$ $m^2\,s^{-1}$ and $D_{z^2} = 7.349\times10^{-11}$ $m^2\,s^{-1}$ for Ni and $D_{x^2+y^2} = 2.902\times10^{-10}$ $m^2\,s^{-1}$ and $D_{z^2} = 3.028\times10^{-10}$ $m^2\,s^{-1}$ for Y. Against our expectation, the horizontal and the vertical mean square displacements do not differ from each other.

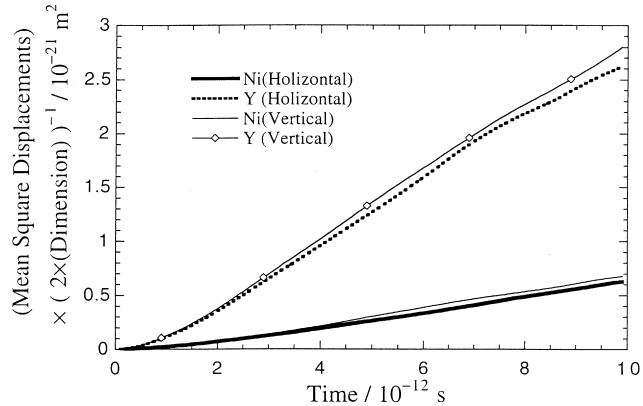

Fig. 9. Mean square displacements (MSD) at 773 K. The solid line shows a horizontal MSD in the Ni, the dashed line shows a horizontal MSD for Y, the thin line shows a vertical MSD for Ni and the thin line with open square markers shows a vertical MSD for Y.

The possible reason for this is that the high rate diffusion does occur in the grain-boundary region, but that the range that enables large diffusivity is wider than expected.

An additional 3000 time steps calculation with higher sampling rates of coordinates is performed for two reasons; to see the atomic arrangements after sufficiently long time steps through radial distribution function, and to calculate the spectral densities of velocity with sufficiently good precision.

In Fig. 10 the radial distribution function for the grain-boundary structure calculated for the additional 3000 time steps is shown. The obtained curves are not as smooth as those in Fig. 3, but the sharp peaks structure can be observed for all distributions except for the Y–Y pair distribution. The distribution function for Y–Y shows that the structure of Y is disordered although we adopted a larger r_{cut} than those for the other two types of interactions. This is also the case for the preliminary 2000 steps calculation with larger cut off lengths. Most of the peaks observed are the same as those observed for the perfect crystal structure, but one extra peak is visible for each distribution in the short range. For the perfect crystal structure, such short interatomic separations are unfavourable because of the strong repulsive interactions (see Fig. 2). This one extra peak is also observed for the preceding 10 000 time steps simulation. This may be the one for the relaxed short separations set in the initial configuration. As we can see, they do not vanish even after 10 ps, which is characteristic for the atomic jump calculated with Fig. 9 and the crystallographic separations. These short interatomic separations can be possible probably because we have used the direct many-body attractive force calculation. The integrated values around each of the peaks at the first-nearest-neighbour are 6.6(Ni–Ni), 7.3(Ni–Y) and 4.2(Y–Y), respectively, as those for the crystallographic perfect crystal structures are 6(Ni–Ni), 8(Ni–Y) and 4(Y–Y).

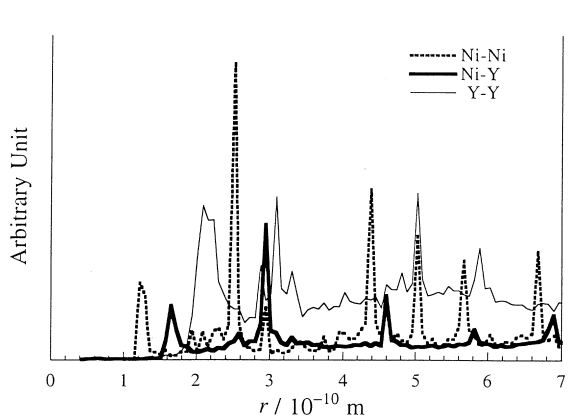

Fig. 10. Radial distribution function for the grain-boundary structure at 773 K calculated from 1/10 sample coordinates in additional 3000 time steps simulation. The dashed line shows the Ni–Ni pair distribution, the bold solid line shows the Ni–Y pair distribution and the thin solid line shows the Y–Y pair distribution.

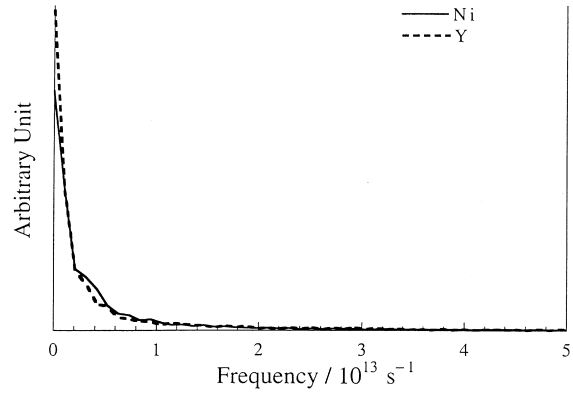

Fig. 11. Spectral densities of velocity for Ni and Y at 773 K in the grain-boundary structure calculated from 1/10 sample velocities in additional 3000 time steps simulation. The solid line is for Ni and the dashed line is for Y.

The diffusive motion is also observed as the zero frequency mode in the spectral densities shown in Fig. 11.

Presented in Fig. 12 are the plots of the self-diffusion coefficients of both horizontal and vertical motions. It proves that the rate of the self-diffusion becomes higher when atoms are near the grain-boundary but the values themselves remain high throughout the simulation cell size used in this model.

4. Conclusions

We have carried out a molecular dynamics simulation on the Ni_2Y intermetallic phase with a nearly-free-electron–tight-binding-bond interatomic interaction model.

The ordered structure was reproduced for the several structure models for this intermetallic phase.

High rate self-diffusion phenomena has only been

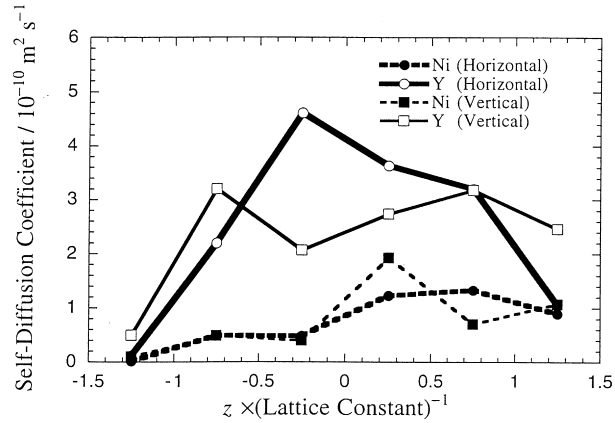

Fig. 12. Variation of the horizontal and the vertical self-diffusion coefficients versus z axis neutral to the grain-boundary. The bold lines represent the horizontal self-diffusion coefficients and the thin lines represent the vertical self-diffusion coefficients. For both the coefficients, the dashed lines represent Ni and the solid lines represent Y.

observed in the symmetrical grain-boundary model among three structure models, and we have concluded that the high growth rate of the Ni_2Y phase accomplished in the electrochemical experiments is due to the high diffusion rate in and near the grain-boundaries.

The dynamical structure of our Ni vacancy structure model made no significant difference from a perfect crystal structure model. Therefore, we have found it difficult to ascribe the cause of the high growth rate to the standard vacancy model of diffusion.

Acknowledgements

Most of the computations in the present study were done on CRAY T94/4128 at the Institute for Chemical Research, Kyoto University.

References

[1] G. Xie, K. Ema, Y. Ito, J. Appl. Electrochem. 24 (1994) 321.
[2] P. Egelstaff, An Introduction to the Liquid State, Academic Press, London, 1967.
[3] P.G. Shewmon, Diffusion in Solids, McGraw-Hill, New York, 1963.
[4] D.G. Pettifor, Bonding and Structure of Molecules and Solids, Oxford University Press, Oxford, 1995.
[5] Ch. Hausleitner, J. Hafner, Phys. Rev. B 45 (1992) 115.
[6] D.G. Pettifor, M.A. Ward, Solid State Commun. 49 (1984) 291.
[7] N.W. Ashcroft, Phys. Lett. 23 (1966) 48.
[8] A.P. Sutton, M.W. Finnis, D.G. Pettifor, Y. Ohta, J. Phys. C 21 (1988) 35.
[9] J.M. Wills, W.A. Harrison, Phys. Rev. B 28 (1983) 4363.
[10] H. Yamada, J. Inoue, K. Terao, S. Kanda, M. Shimizu, J. Phys. F 14 (1984) 1943.
[11] D.G. Pettifor, M. Aoki, Philos. Trans. R. Soc. London, Ser. A 334 (1991) 439.
[12] D.G. Pettifor, in: R.M. Nieminen, M.J. Puska, M.J. Manninen (Eds.), Many-Atom Interactions in Solids, Springer-Verlag, Berlin, 1990, p. 64.
[13] W.A. Harrison, Electronic Structure and the Properties of Solids, Freeman, San Francisco, 1980.
[14] D. Nguyen-Manh, D. Mayou, A. Pasturel, F. Cyrot-Lackmann, J. Phys. F 15 (1985) 1911.
[15] S. Nosé, J. Chem. Phys. 81 (1984) 511; Mol. Phys. 52 (1984) 255.
[16] W.G. Hoover, Phys. Rev. A 31 (1985) 1695.
[17] B.L. Holian, A.F. Voter, R. Ravelo, Phys. Rev. E 52 (1995) 2338.
[18] D.A. McQuarrie, Statistical Mechanics, Harper Collins, New York, 1976.
[19] M.P. Allen, D.J. Tildesley, Computer Simulation of Liquids, Oxford University Press, Oxford, 1987.
[20] K. Hachiya, Y. Ito, unpublished data.
[21] W.G. Hoover, Computational Statistical Mechanics, Elsevier, Amsterdam, 1991.